

Article

Unusual Lattice Parameters Behavior for $\text{La}_{1.9}\text{Ca}_{0.1}\text{NiO}_{4+\delta}$ at the Temperatures below Oxygen Loss

Denis Mishchenko ¹, Zakhar Vinokurov ^{1,*}, Evgeny Gerasimov ², Elena Filonova ³, Alexander Shmakov ¹ and Elena Pikalova ^{4,5}

¹ Synchrotron Radiation Facility SKIF, Boreskov Institute of Catalysis, SB RAS, 630559 Novosibirsk, Russia; q14999@yandex.ru (D.M.); highres@mail.ru (A.S.)

² Federal Research Center Boreskov Institute of Catalysis, SB RAS, 630090 Novosibirsk, Russia; gerasimov@catalysis.ru

³ Department of Physical and Inorganic Chemistry, Institute of Natural Sciences and Mathematics, Ural Federal University, 620002 Yekaterinburg, Russia; elena.filonova@urfu.ru

⁴ Laboratory of Solid Oxide Fuel Cells, Institute of High Temperature Electrochemistry, UB RAS, 620137 Yekaterinburg, Russia; e.pikalova@list.ru

⁵ Department of Environmental Economics, Institute of Economics and Management, Ural Federal University, 620002 Yekaterinburg, Russia

* Correspondence: vinokurovzs@catalysis.ru

Abstract: In this work, we studied the structural features of $\text{La}_{1.9}\text{Ca}_{0.1}\text{NiO}_{4.11}$, which is considered a promising cathode material for intermediate temperature solid-oxide fuel cells (IT-SOFC). The effect of different pretreatments on the structural characteristics of the sample was studied using X-ray diffraction (XRD) and high-resolution transmission electron microscopy (HRTEM) in order to elucidate the origin of a peculiar change of lattice parameters observed earlier during in situ XRD studies. The XRD studies have shown that anisotropic broadening for reflections with a high Miller index l appears after tempering of a quenched (from 1100 °C) sample at 250 °C. This temperature is too low for the release/incorporation of oxygen into the structure but is sufficient for oxygen migration inside the structure. The HRTEM assisted us in revealing differences in the defect structure after different pretreatments. Based on obtained results, the following possible explanation was proposed. Observed additional microstrains and non-oriented planar defects as well as a decrease in the coherent scattering region size in the [001] direction are caused by the non-homogeneous redistribution of interstitial oxygen in the structure during tempering.

Keywords: anisotropic XRD peak broadening; HRTEM; $(\text{La,Ca})\text{NiO}_4$; IT-SOFC; lanthanum nickelates



Citation: Mishchenko, D.; Vinokurov, Z.; Gerasimov, E.; Filonova, E.; Shmakov, A.; Pikalova, E. Unusual Lattice Parameters Behavior for $\text{La}_{1.9}\text{Ca}_{0.1}\text{NiO}_{4+\delta}$ at the Temperatures below Oxygen Loss. *Crystals* **2022**, *12*, 344. <https://doi.org/10.3390/cryst12030344>

Academic Editor: Konrad Świerczek

Received: 8 February 2022

Accepted: 28 February 2022

Published: 2 March 2022

Publisher's Note: MDPI stays neutral with regard to jurisdictional claims in published maps and institutional affiliations.



Copyright: © 2022 by the authors. Licensee MDPI, Basel, Switzerland. This article is an open access article distributed under the terms and conditions of the Creative Commons Attribution (CC BY) license (<https://creativecommons.org/licenses/by/4.0/>).

1. Introduction

Researchers have paid close attention to the classes of complex, layered perovskite-like oxides structurally related to the Ruddlesden-Popper (R-P) [1–3]. A reasonable choice of dopant types and doping level can help to obtain materials with superior properties [4,5]. Among oxides with the R-P structure, a class of first-order phases with a general formula of $\text{Ln}_2\text{NiO}_{4+\delta}$ ($\text{Ln} = \text{La}, \text{Pr}, \text{Nd}$) are considered potential cathode materials for various types of electrochemical cells [6–8] as well as materials for oxygen-permeable membranes [8]. The widespread electrochemical applications of $\text{Ln}_2\text{NiO}_{4+\delta}$ phases are characterised by a number of distinctive features: enhanced mixed ionic-electronic conductivity (MIEC), boosted chemical/thermal stability and mechano-thermal compatibility with electrolyte materials. All the above-mentioned properties made it possible to successfully verify $\text{Ln}_2\text{NiO}_{4+\delta}$ derivatives, substituted with alkaline earth metals (Ca, Sr, Ba) on the Ln-site, as cathode materials in the cells both with oxygen- [6,9–16] and proton-conducting electrolytes [6,16–21].

The uniqueness of the above-mentioned combination of functional properties of $\text{Ln}_2\text{NiO}_{4+\delta}$ is attributed to the presence of highly mobile over-stoichiometric oxygen in

the form of interstitial oxygen ions. From the point of view of quasi-chemistry, interstitial oxygen is usually considered as a point defect O_i'' located in a LnO rock-salt-like layer at the tetrahedral site [22,23]. The accommodation of interstitial oxygen in the lattice relaxes the lattice strain caused by the discrepancy between the dimensional characteristics of perovskite and rock-salt layers in the (*ab*) plane [24]. This strain is usually quantitatively estimated using the Goldschmidt perovskite-structure stability factor (tolerance factor), t [25].

The empirically determined values (excluding certain cases) of the tolerance factor for the considered complex oxides with a tetragonal structure are in the range of $0.87 < t < 1.0$ [24,25]. The more the t factor deviates from unity, the higher the level of lattice strain in the structure, thereby leading, at a certain point, to the formation of less stable orthorhombic structures [24,25]. As the ionic radius of $^{IX}\text{Ln}^{3+}$ decreases in the row La_2NiO_4 - Pr_2NiO_4 - Nd_2NiO_4 , the t factor decreases, which means that more excess oxygen is required to reduce the lattice strain [26].

For the stoichiometric La_2NiO_4 , the t value calculated from the ionic radii data given in [27] is equal to 0.885, which indicates the tensile stress experienced by the La–O bonds while the Ni–O bonds experience compressive stress [6]. The accommodation of interstitial oxygen into the La_2NiO_4 lattice leads to a weakening of stresses of both types for two reasons [6]. Firstly, due to the La–O bond length increase caused by an increase in the coordination number of La^{3+} ; secondly, due to the Ni–O bond-length decrease caused by the partial oxidation of Ni^{2+} ions to Ni^{3+} ions (the latter having a smaller ionic radius [27]) in order to satisfy the electroneutrality condition. Additionally, it is possible to stabilize the structure by the partial substitution of La^{3+} ions by alkaline earth metal ions M^{2+} ($\text{M} = \text{Ca}, \text{Sr}, \text{Ba}$) which leads to a significant increase in the tolerance factor t at high dopant concentrations as clearly illustrated in [28].

The incorporation of over-stoichiometric oxygen into the La_2NiO_4 structure and substitution of the La^{3+} ion by the alkaline earth metal ion M^{2+} both lead to the formation of electron holes (h) in the oxide structure [29,30]. The concentration of electron holes mainly determines the superior electronic conductivity of the considered materials [31]. Nevertheless, oxygen-transport properties and ionic conductivity deteriorate with doping as demonstrated in a number of studies [32–36]. It was shown in [37] that in the $\text{La}_{2-x}\text{M}_x\text{NiO}_{4+\delta}$ ($\text{M} = \text{Ca}, \text{Sr}, \text{Ba}$) series, doping with an alkaline earth metal (12.5 mol%) increases migration energy barriers and also alters the migration energy ratio between different interstitial oxygen-diffusion paths. However, from an energetic point of view, Ca-doping is less destructive to oxygen transport compared to doping with Ba or Sr. Moreover, Ca-doping in a low amount (5 mol%) was shown to facilitate the oxygen-transport properties compared to undoped $\text{La}_2\text{NiO}_{4+\delta}$ [36].

Furthermore, $\text{La}_{2-x}\text{Ca}_x\text{NiO}_{4+\delta}$ complex oxides, exhibiting a tetragonal structure in the entire range of the dopant concentrations up to the solubility limit (~25 mol%), were previously studied in [28,36,38–40]. The tolerance factors for $\text{La}_{1.9}\text{Ca}_{0.1}\text{NiO}_{4+\delta}$ calculated for stoichiometric composition ($\delta = 0$) and for composition with $\delta = 0.11$ [36] are equal to 0.889 and 0.897, respectively, and illustrate the increasing stability of the oxide structure in the case of both excess interstitial oxygen accommodation and substitution of lanthanum by calcium.

In our previous work [36], an unusual behavior of the $\text{La}_{1.9}\text{Ca}_{0.1}\text{NiO}_{4.11}$ sample was observed. The sample exhibited a structure unexpectedly more stable than it was assumed to be from the calculations of the dependence of δ on Ca content. In addition, according to thermogravimetric data, the $\text{La}_{1.9}\text{Ca}_{0.1}\text{NiO}_{4.11}$ sample was found to have the highest temperature of oxygen loss in the $\text{La}_{2-x}\text{Ca}_x\text{NiO}_{4+\delta}$ series. The decrease in the δ value for $\text{La}_{1.9}\text{Ca}_{0.1}\text{NiO}_{4.11}$ affected the concentration of charge carriers: this sample had the lowest content of Ni^{3+} ions in the series (32% at 25 °C in air). A similar minimum of the Ni^{3+} content in the $\text{La}_{2-x}\text{Ca}_x\text{NiO}_{4+\delta}$ series was observed in [34] for the sample $\text{La}_{1.9}\text{Ca}_{0.1}\text{NiO}_{4.08}$ (26% at 25 °C in air).

In order to elucidate the reasons behind the above-mentioned peculiarities of the $\text{La}_{1.9}\text{Ca}_{0.1}\text{NiO}_{4.11}$ (LCNO_01) sample, we performed a structural study of the sample during different thermal treatments.

2. Materials and Methods

2.1. Synthesis

The LCNO_01 material for the study was prepared using a nitrate combustion method from the starting materials of $\text{Ni}(\text{NO}_3)_2 \cdot 4\text{H}_2\text{O}$ (>99% of purity), $\text{Ca}(\text{NO}_3)_2 \cdot 4\text{H}_2\text{O}$ (>98.5%) and $\text{La}(\text{NO}_3)_3 \cdot 6\text{H}_2\text{O}$ (99.99%) according to the procedure described in detail elsewhere [36]. As a fuel, a mixture of glycine and glycerol in a ratio of 1.5:0.5 to nitrate groups was taken. After combustion, the resulting powder was stepwise calcinated at 500 °C, 1000 °C and 1150 °C for 5 h at each temperature. The heating/cooling rate of a high-temperature furnace LHTC 08/16 used for sintering (Nabertherm, Lilienthal, Germany) was 150°/h. The intermediate and final ball-milling of the powder was performed using a Pulverisette 6 planetary mill (Fritsch, Idar-Oberstein, Germany).

2.2. XRD

The in situ XRD study of the as-prepared powdered sample (LCNO_01) was performed at the High Precision Diffractometry II station at the synchrotron radiation facilities of the VEPP-3 storage ring (the Siberian Synchrotron and Terahertz Radiation Centre, Novosibirsk, Russia) [41]. A wavelength of 0.10095 nm was established using a flat Si(220) crystal. The station diffractometer was equipped with a position-sensitive parallax-free linear OD-3M detector [42] with a working range of approximately 30° and a 2 θ resolution of approximately 0.01°. The exposition time was 60 s per pattern. The as-prepared LCNO_01 sample was heated/cooled at a rate of 10 °C/min, first in helium (He) flow, then in synthetic air flow in a temperature range of 30–700 °C using a XRK900 reactor (Anton Paar, Graz, Austria). The gas flow rate was 100 sccm in both cases.

The in situ XRD study of the LCNO_01 sample quenched from 1100 °C to RT (room temperature), assigned as LCNO_01_q, was performed using a Bruker D8 Advance diffractometer equipped with a Lynxeye linear detector (Bruker, Bremen, Germany). The diffraction patterns were obtained in a $\theta/2\theta$ configuration using Ni-filtered $\text{CuK}\alpha$ radiation ($\lambda = 0.15418$ nm). In situ diffraction patterns were recorded during the stepwise heating/cooling in a temperature range of 30–500 °C with a step of 25 °C in 100 sccm He flow using a XRK900 chamber. A fixed 2 θ configuration was used in a range from 41.8 to 44.7°, with a step of 0.015° and an exposition time of 120 s. At RT, the sample was scanned in a 2 θ range from 27 to 80° with a step of 0.02° and a counting time of 3 s at each point.

The phases were identified using the powder-diffraction database PDF-4+. The refinement of the crystal structure was performed with the Rietveld method using GSAS-II software packages [43].

2.3. HRTEM

The morphology and phase composition of the samples were investigated using a ThemisZ electron microscope (Thermo Fisher Scientific, Waltham, MA, USA) equipped with a corrector of spherical aberrations, at an accelerating voltage of 200 kV. The images were recorded using a Ceta 16 CCD sensor (Thermo Fisher Scientific, MA, USA), while the samples for the HRTEM study were prepared on a holey carbon film mounted on a copper grid via the ultrasonic dispersing of the samples' suspension in ethanol.

2.4. TGA

Thermogravimetric analysis of the LCNO_01_q sample was conducted using an NETZSCH STA 449 C Jupiter device (Netzsch, Selb, Germany).

The measurement was carried out in helium flow (20 sccm) in a temperature range from 50 to 700 °C at a heating rate of 10 °C/min.

3. Results and Discussion

An XRD study of the as-prepared LCNO_01 sample at RT was performed earlier [36]. It was shown that the sample possesses a tetragonal K_2NiF_4 -type structure ($I4/mmm$ sp.gr.). The Rietveld-refinement results of the initial structure are shown in Table 1. Unusual behavior of the lattice parameters was registered during thermal and chemical stability study of this sample by in situ SXRD (Figure 1a). A strong antipate change of a and c lattice parameters in a temperature range from approximately 200 °C to 450 °C was observed during heating of the as-prepared sample in He flow. In contrast, linear behavior of parameters was observed during cooling with a slope change point occurring around 400 °C. It is worth mentioning that during heating, despite a strong parameter change, the cell volume showed behavior close to linear (Figure 1b). Therefore, changes in the a and c parameters compensated for one other. It should also be noted that similar behavior was observed for samples $La_2NiO_{4.17}$ and $La_{1.8}Ca_{0.2}NiO_{4.09}$ (which was also studied in [36], Figures S1 and S2) but with a substantially lower magnitude of parameter change.

Table 1. Results of Rietveld refinement of LCNO_01 structure at RT.

Parameters ¹	LCNO_01 as Prepared [36]	LCNO_01_q after Quenching (From 1100 °C to RT)	LCNO_01_t after 250 °C (He, 150 min)	LCNO_01_700 after 700 °C (Air, 20 min)
a , Å	3.8509 (5)	3.8523 (1)	3.8547 (2)	3.8520 (1)
c , Å	12.644 (1)	12.6427 (6)	12.617 (1)	12.6481 (6)
V , Å ³	187.50 (1)	187.62 (2)	187.48 (4)	187.67 (2)
U (La/Ca)	0.0121 (4)	0.0128 (4)	0.0107 (4)	0.0128 (3)
z (La/Ca)	0.361 (1)	0.361 (1)	0.362 (1)	0.361 (1)
U (Ni)	0.012 (1)	0.0142 (7)	0.0148 (9)	0.0149 (7)
U (O eq.)	0.015 (3)	0.025 (2)	0.027 (3)	0.024 (2)
occ. (O eq.)	1.00	1.00	1.00	1.00
U (O ap.)	0.042 (3)	0.042 (2)	0.029 (3)	0.038 (2)
z (O ap.)	0.174 (1)	0.174 (1)	0.177 (1)	0.174 (1)
occ. (O ap.)	1.00	1.00	1.00	1.00
U (O int.)	0.042 (3)	0.042 (2)	0.029 (3)	0.038 (2)
occ. (O int.)	0.09 (2)	0.07 (1)	0.06	0.08 (1)
			S_{400}^2	
			34,500 (1200)	
			S_{004}	
microstrain, $\Delta d/d \cdot 10^{-6}$	907 (76)	889 (32)	1400	692 (27)
			S_{220}	
			39,100 (1600)	
			S_{022}	
			−200	
δ	0.18 (4)	0.14 (2)	0.12	0.16 (2)
wR, %	11.72	3.73	4.94	3.88
GoF	2.6	1.28	1.58	1.53

¹ U—thermal XRD factor; O eq.—equatorial position in oxygen octahedron; O ap.—apical position in oxygen octahedron; O int.—tetrahedral interstitial oxygen position; occ.—occupancy of an atomic site; values without uncertainties were fixed during refinement. ² Stephens [44].

The Rietveld refinement results of the LCNO_01 structure after different treatments (described below) are presented in Table 1, while the corresponding refinement profiles are presented in supplementary information (Figures S3–S6).

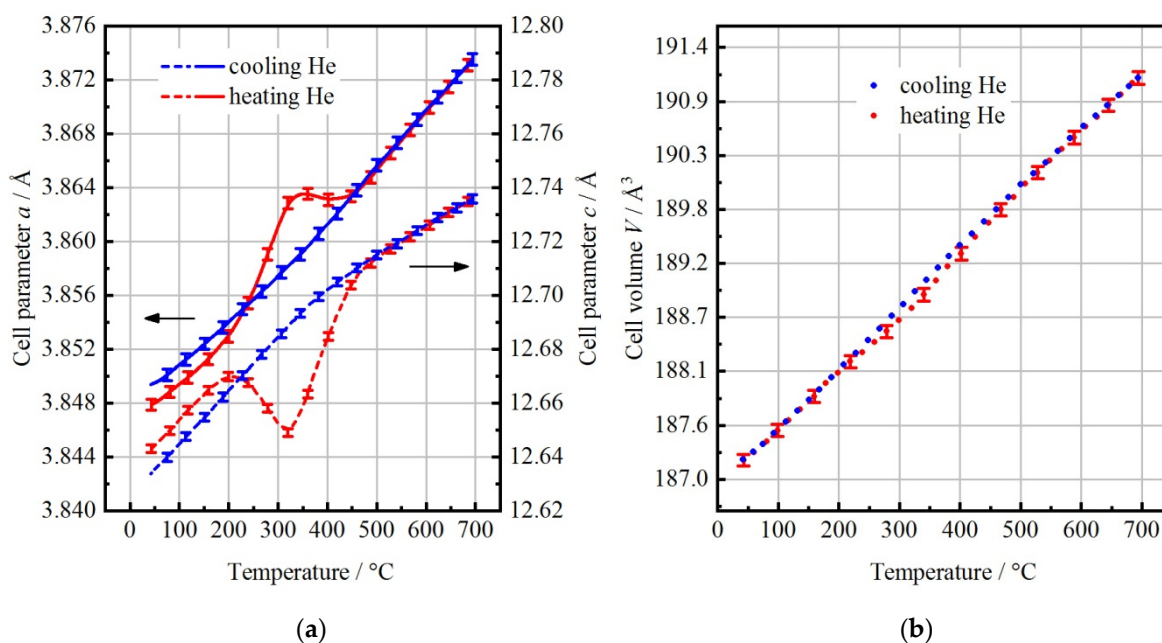


Figure 1. Lattice parameters a , c (a) and volume (b) as a function of temperature, obtained from XRD patterns for LCNO_01 collected in He flow.

It was found that such a behavior of lattice parameters is observed only in the as-prepared sample, and any high-temperature treatment (higher than approximately 200 °C) with a relatively slow cooling rate leads to its disappearance. To reproduce such a change in the lattice parameters, we heated the sample to 1100 °C in air and quenched it down to RT (sample designated LCNO_01_q). The annealing temperature was chosen to be 50 °C lower than the final synthesis temperature.

According to the XRD data, the quenched sample does not show any structural stresses or superstructural reflections (Figure S4) however, we were able to reproduce the strong antilate behavior of lattice parameters similar to that observed in the initial LCNO_01 (Figure 2a).

To prove that lattice-parameter change is caused not by oxygen loss but by oxygen migration in the structure, we heated the quenched sample in He up to 250 °C, which is 150 °C lower than the temperature of oxygen loss according to the TGA data collected in an inert atmosphere (Figure S7) and 50 °C higher than the activation temperature of oxygen diffusion according to the isotope-exchange data (TPIE) [36]. In static conditions for 150 min of annealing at 250 °C, we observed a decrease in the c parameter and an increase in the a parameter (Figure 2b), both of which were expected based on Figures 1a and 2a.

It is interesting that after cooling, apart from the shortening of the c parameter and the expansion of the a parameter, the sample exhibited highly anisotropic microstrains in a crystallographic direction [001] (Figure 3a). As it can be seen from Figure 3b, there is a distinct broadening of the reflections with 001 and hkl (for high l and low h/k) Miller indices compared to the reflections in the quenched sample. A generalized model proposed by Stephens [44] to treat the anisotropic broadening of reflections provides a satisfactory fit that can be illustrated by a comparison of the observed FWHM of the individual peaks with those calculated using the anisotropic model (Figure 3b). Figure 3c shows two separate Williamson-Hall fits for the broadened reflections and other reflections. This plot clearly shows a lessening of the coherent scattering region (CSR) in the [001] direction (higher intersection of Y -axis) as well as an increase in the microstrains (bigger slope of the fitted line for broadened reflections).

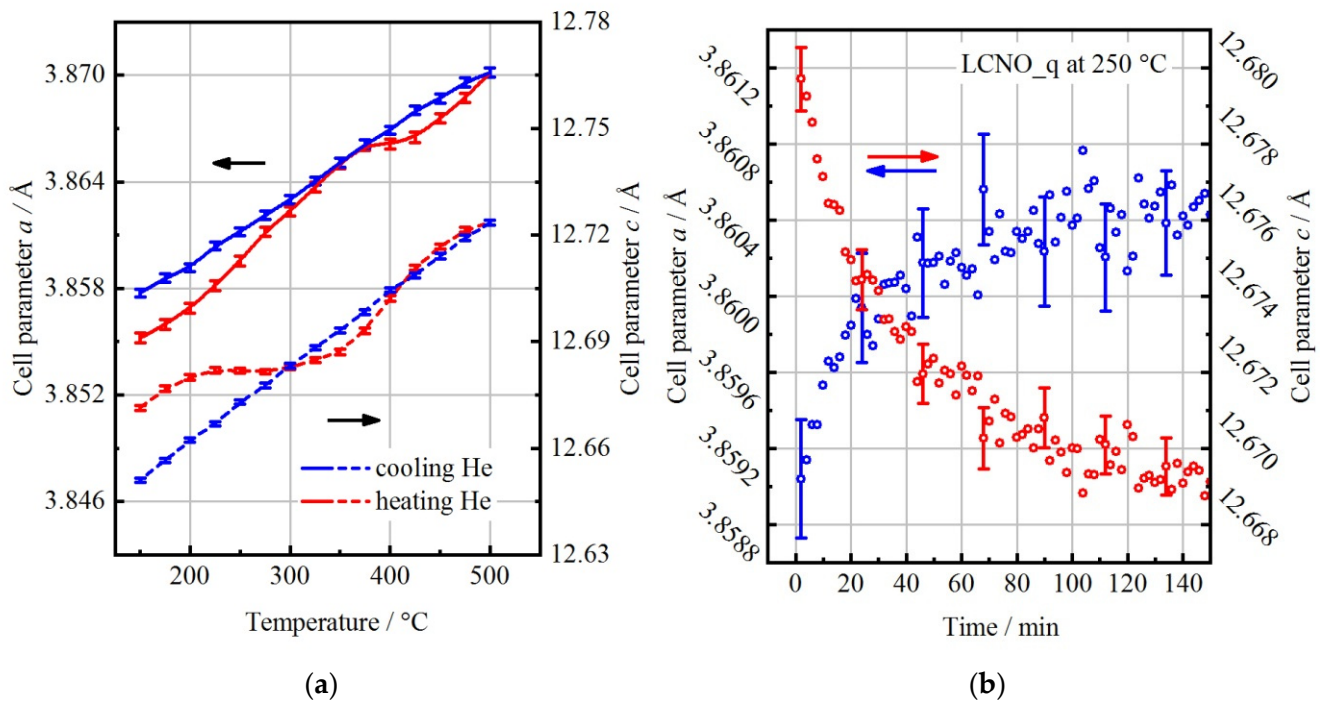


Figure 2. Lattice parameters a , c as a function of temperature—(a), as a function of time at 250 °C—(b) obtained from XRD patterns for LCNO_01_q in He flow.

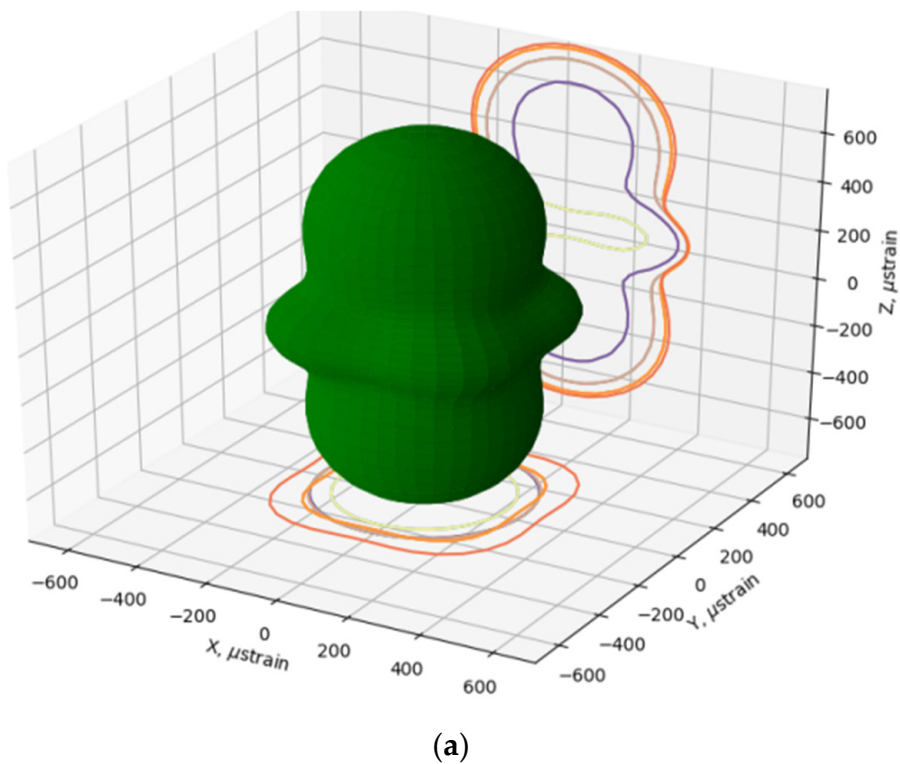


Figure 3. Cont.

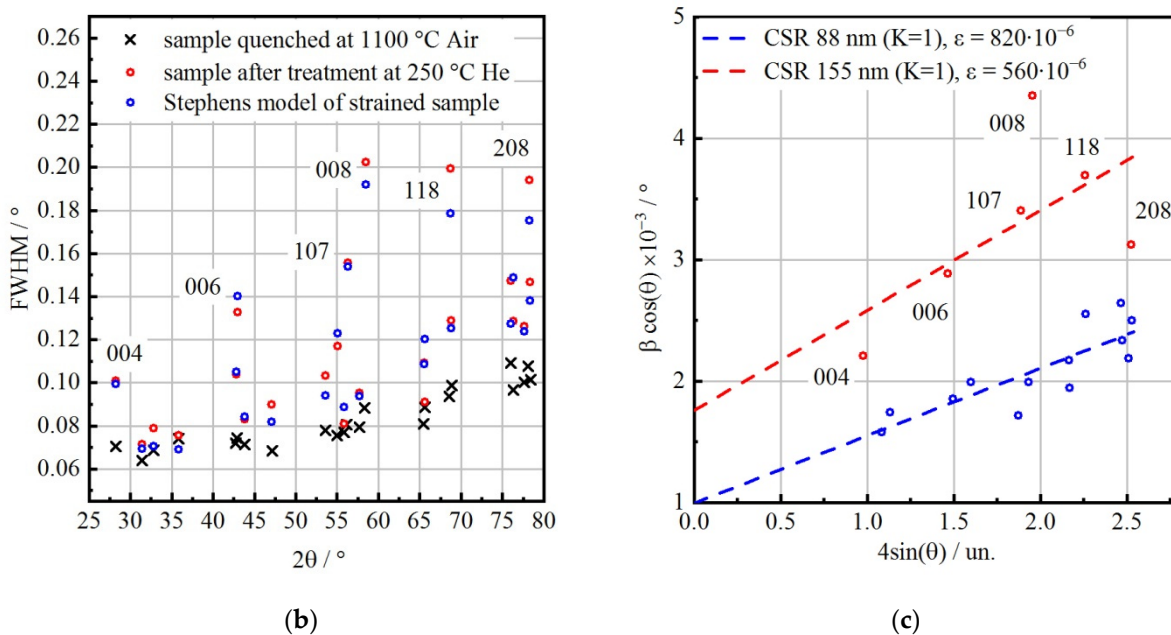


Figure 3. Three-dimensional strain distributions derived from Stephens’s model [44] in GSAS-II software [43] for LCNO_01_q after treatment in He at 250 °C (LCNO_01_t)—(a); FWHM versus 2θ for experimental diffraction profiles LCNO_01_q (black crosses), LCNO_01_t (red circles) and for fitted diffraction profile (blue circles, Stephens’s model [44])—(b); Williamson Hall plot for 00l and hkl (for high l and low h/k) reflections (red circles) and others reflections (blue circles) for LCNO_01_t sample—(c). β —integral breadth.

Figure 4 illustrates the improvement of the Rietveld fit when using Stephens’s model compared to the one fitted using isotropic broadening approximation ($\epsilon = 2200 \times 10^{-6}$) for the tempered sample LCNO_01_t.

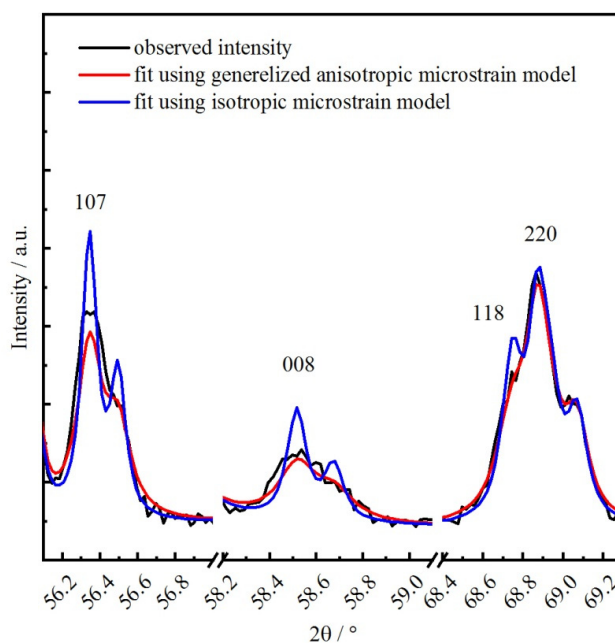


Figure 4. Comparison of the Rietveld fit for 107, 008 and 118 reflections between the isotropic and anisotropic microstrain models (implemented in GSAS-II software [43]) derived for LCNO_01_t. CuK_α radiation.

There are other studies in which anisotropic broadening of XRD reflections for layered perovskite-like phases was also observed. One of the first mathematical treatments of anisotropic broadening was suggested by Rodriguez-Carvajal et al. [45] while analyzing the effect caused by a low-temperature (80 K) phase transition in La_2NiO_4 . Later, this model was implemented in FULLPROF software [46]. Stephens [44] expanded the model of anisotropic peak broadening in powder diffraction and implemented this in GSAS-II software [43].

In thin films, anisotropic broadening is caused by stacking faults in the [001] direction, which usually corresponds to a local thickness variation of the perovskite layers [47,48]. For bulk materials, this kind of behavior is observed less frequently, and its origin is not explained in detail. At most, it is mentioned briefly as an observation and dealt with only by fitting experimental data using an anisotropic microstrain model. For example, anisotropic broadening of peaks with a strong Miller index l was observed for $\text{Ln}_{3-x}\text{Sr}_{1+x}\text{CrNiO}_{8-\delta}$ [49]. The closest case to the one discussed at hand is for $\text{La}_{2-x}\text{Sr}_x\text{Ni}_{1-y}\text{Fe}_y\text{O}_{4+\delta}$ [50], where broadening was observed for reflections with the Miller indices type of 002^*n , $n = 1, 2, 3, \dots$. Importantly, the sample in that work was synthesized with the last step being quenching from 1100 °C to an RT. Aguadero et al. observed similar features for the XRD profile of LaSrNiO_4 , however, they used a two-phase model with a slightly different parameters to improve the fit [51].

It seems that such an effect usually occurs for non-equilibrated R-P phases and might be caused by the inherent anisotropy of their structure. However, what actually happens on the atomic level is difficult to deduce from XRD data since it provides an atomic structure averaged across the whole probed sample volume. Of particular importance is the fact that the observed microstrains appear after treating the sample at the temperature of oxygen diffusion activation according to the isotope-exchange data [36] but lower than oxygen release/incorporation by the TGA data (Figure S7). We can propose, from the results obtained, that microstrains, which appear mainly in the [001] direction, are probably caused by a non-homogeneous redistribution of the interstitial oxygen. This non-homogeneity arises in order to reduce the lattice strain, which was not compensated during quenching from high-temperature state (it has lesser strain due to expansion of the lattice). The redistribution is uneven because the sample cannot insert new interstitial oxygen since the temperature is not high enough to overcome the energy barrier. The resulting distribution likely causes a local distortion of the crystal structure of oxygen octahedrons around nickel atoms. Therefore, we consider the oxygen distribution to be the result of the relaxation of metastable state after quenching. It leads to the interesting behaviour observed of lattice parameters upon tempering because of the impossibility of incorporating more oxygen as it would have happened if it was cooled slowly.

In an attempt to obtain insights into this state on the local level, we used HRTEM applied to the sample in three different states: quenched from 1100 °C (LCNO_01_q), tempered at 250 °C for 150 min (LCNO_01_t), and calcined for 1 h at 500 °C in air (rate of heating/cooling 10 °C/min, LCNO_01). The EDS mapping of the LCNO_01_q sample shows homogeneous distribution of the elements (La, Ca, Ni) over the sample particles (Figure S8a,b).

The HRTEM images of LCNO_01_q sample show well-ordered crystal lattices (Figures 5a and S9a) of micron-sized crystallites with occasionally separated stacking faults (Figures 5b and S9b) which is expected considering the existence of higher-order R-P phases. Overall, the sample after quenching maintains a well-ordered high-temperature relaxed structure which should be metastable at RT.

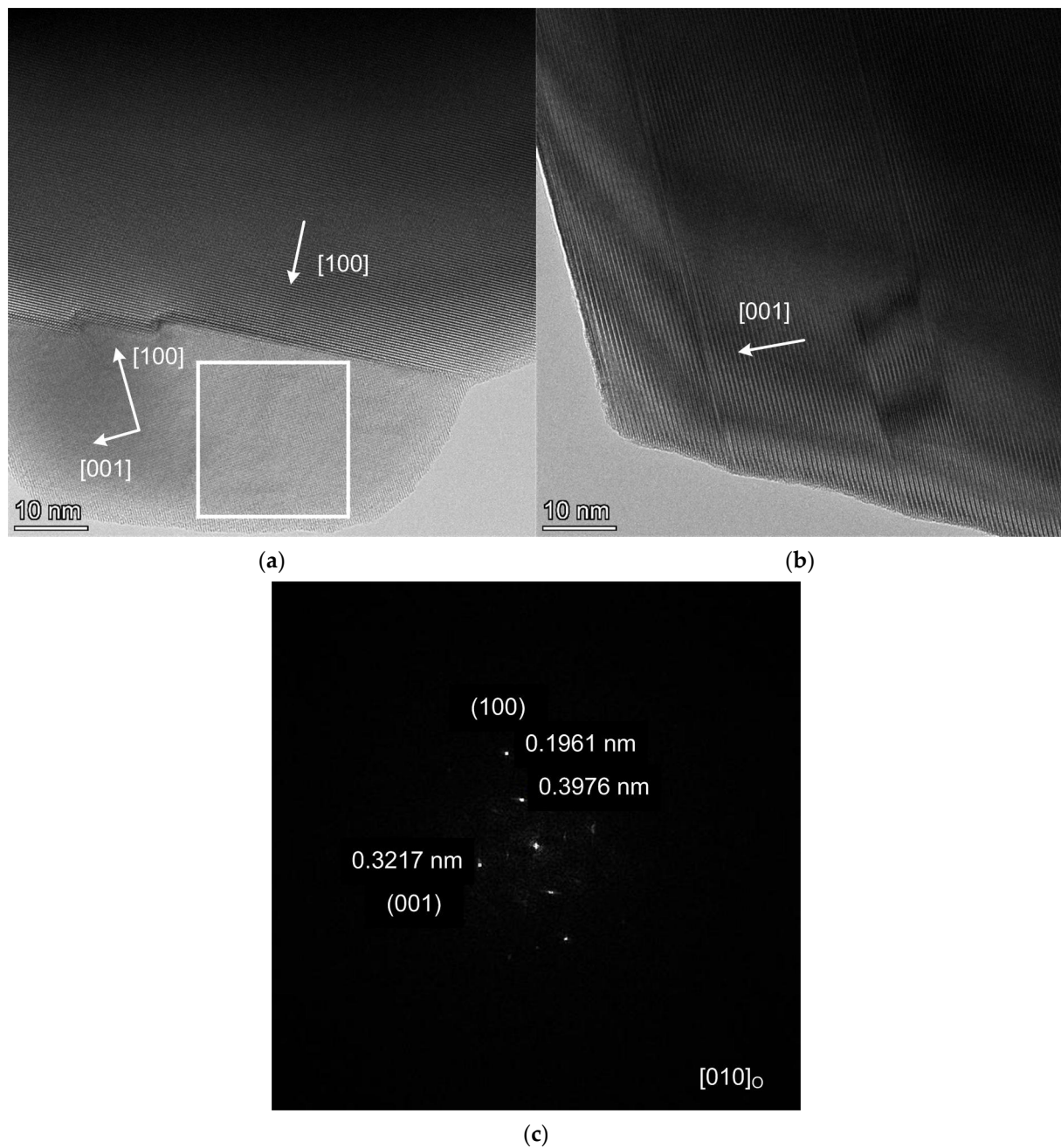


Figure 5. HRTEM image of LCNO_01_q sample—(a); occasional stacking faults in the lattice of LCNO_01_q sample—(b); FFT image of LCNO_01_q from (a) (area marked by white square, zone axis [010])—(c).

The lattice of LCNO_01_t sample is fairly less ordered than that of the quenched one (Figures 6a,b and S10a,b). Moreover, there is some amorphization on the surface and the occurrence of nano-sized particles (presumably NiO) as well as a lot of disorientated planar defects. The FFT image also shows diffuse scattering (elongated shapes of spots) (Figure 6d) and microstrains (enlarged spots sizes) (Figure 6c).

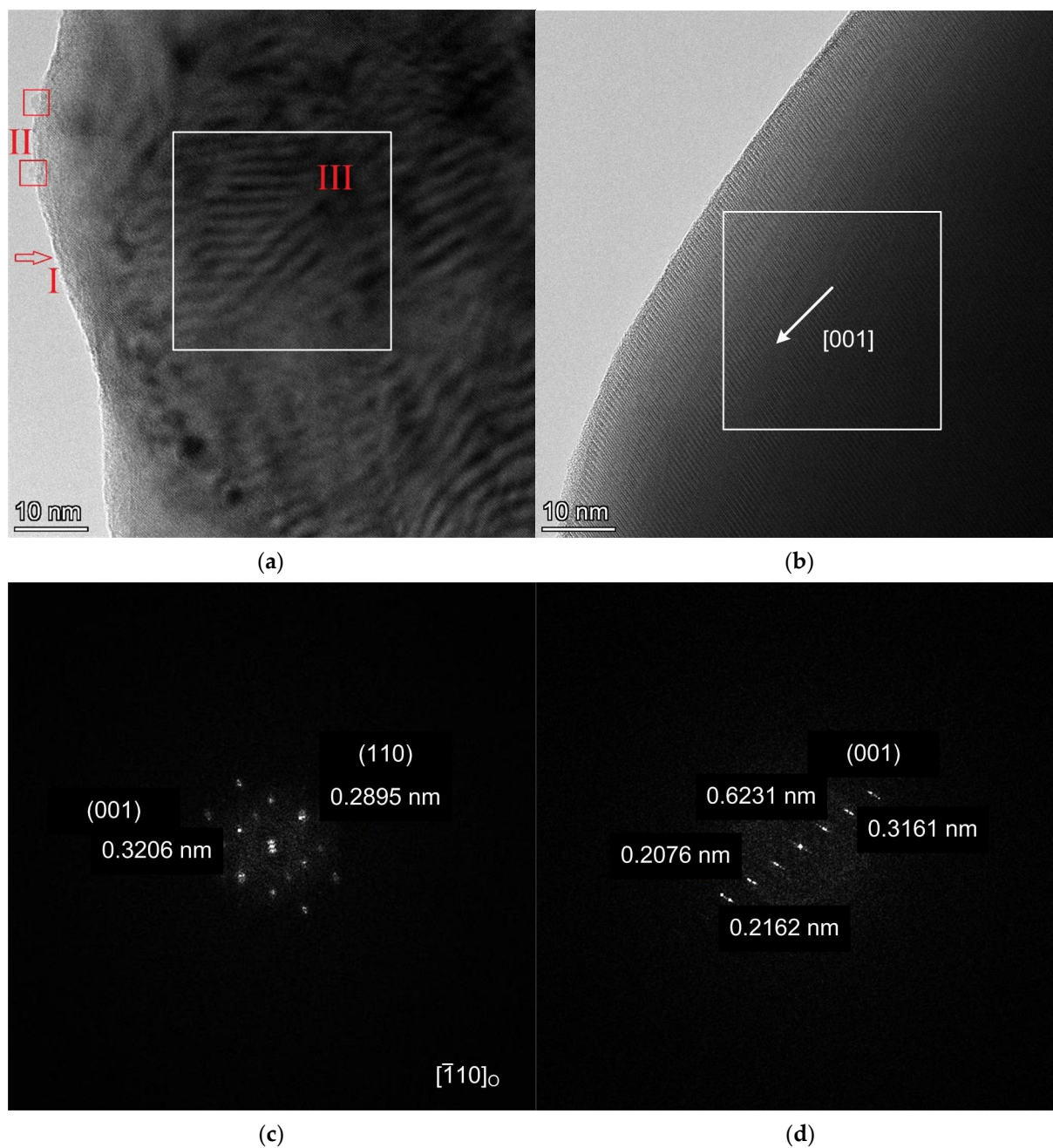


Figure 6. HRTEM images of LCNO_01_t sample (I—amorphization on the surface; II—nano-sized particles on the surface; III—disorientated planar defects)—(a,b); FFT image of LCNO_01_t sample from (a) (area marked by white square, zone axis $[\bar{1}10]$) showing microstrains—(c); FFT image of LCNO_01_t sample from (b) (area marked by white square, zone axis $[110]$) showing diffuse scattering—(d).

The LCNO_01 sample shows a number of planar defects as well (Figures 7a,b and S11a,b) but ordered in the $[101]$ direction (Figure 7c).

To sum up, the HRTEM data confirms a higher level of structural disorder in the LCNO_01_t sample. In contrast to the XRD study, the difference between the LCNO_01_q and LCNO_01 samples, i.e., the presence of orientated defects in the latter, can also be elucidated with this method.

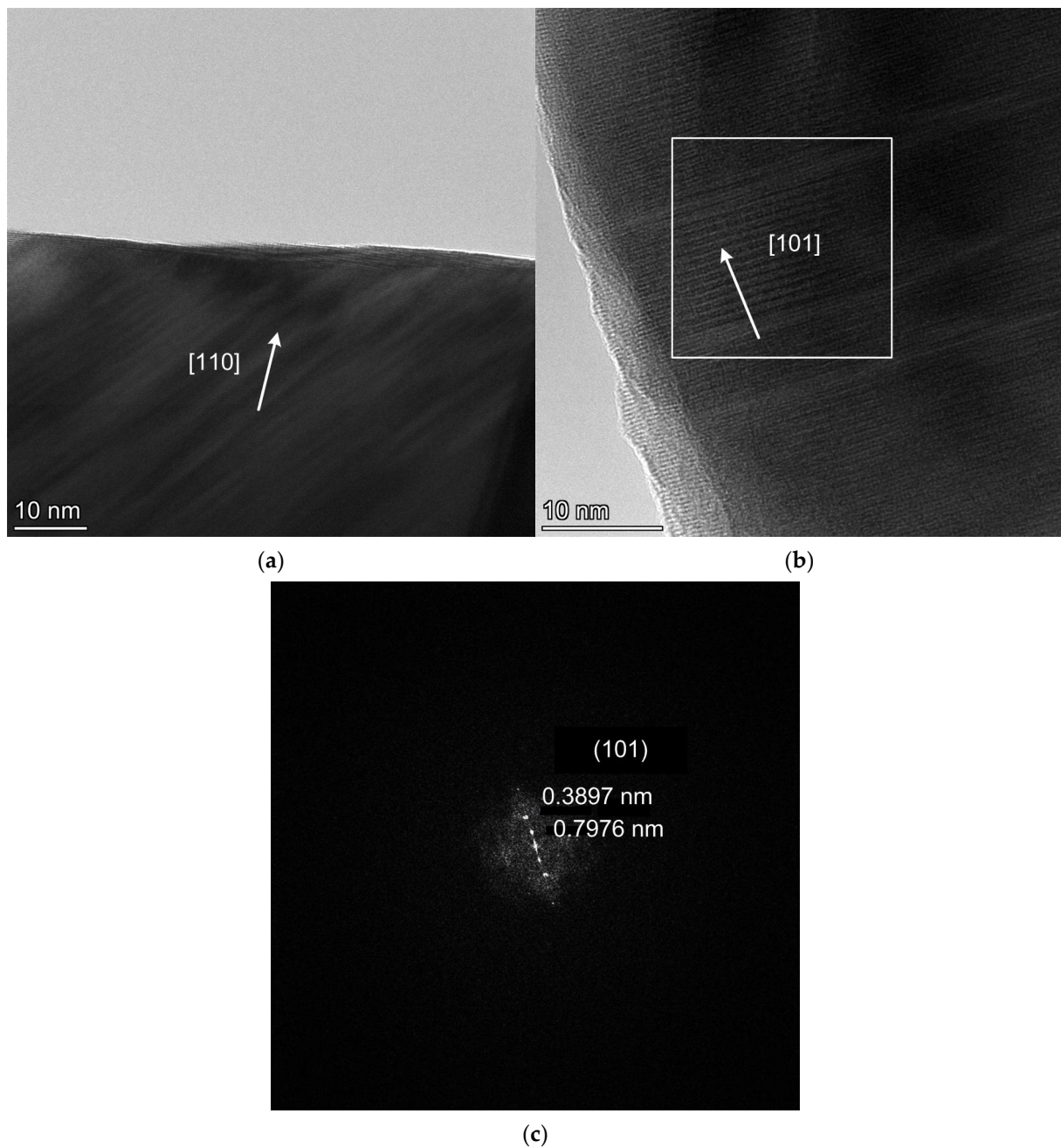


Figure 7. HRTEM images of LCNO_01 sample showing ordered planar defects—(a,b); FFT image of LCNO_01 sample from (b) (area marked by white square) showing orientation of planar defects—(c).

4. Conclusions

In this work, we attempted to obtain structural insight into the peculiar lattice-parameter behaviour of a $\text{La}_{1.9}\text{Ca}_{0.1}\text{NiO}_{4.11}$ sample, a potential IT-SOFC cathode material. We successfully managed to reproduce the behaviour of the parameters and demonstrated that it occurs during the relaxation of the metastable state obtained by quenching from a high temperature. Low-temperature tempering causes a transformation of this state to a new one, with a non-homogeneous distribution of interstitial oxygen in the structure compensating for the lattice strain. This assumption, based on a general understanding of the possible behaviour of the studied complex oxides, was supported by TGA, TPIE, in situ and ex situ XRD (the latter showed anisotropic broadening of reflections in the $[001]$ direction in the tempered sample). Confirmation and further insight on the local level

was provided by HRTEM, which directly revealed a disordered state of the structure after tempering. Moreover, HRTEM indicated the difference between a highly ordered state of the quenched sample and slowly cooled sample with orientated planar defects.

Supplementary Materials: The following supporting information can be downloaded at: <https://www.mdpi.com/article/10.3390/cryst12030344/s1>, Figure S1: Lattice parameters a , c (a) and volume (b) as a function of temperature, obtained from XRD patterns for $\text{La}_2\text{NiO}_{4.17}$ collected in He flow; Figure S2: Lattice parameters a , c (a) and volume (b) as a function of temperature, obtained from XRD patterns for $\text{La}_{1.8}\text{Ca}_{0.2}\text{NiO}_{4.09}$ collected in He flow; Figure S3: Rietveld refinement results of as-prepared LCNO_01 sample; Figure S4: Rietveld refinement results of quenched LCNO_01_q sample; Figure S5: Rietveld refinement results of tempered LCNO_01_t sample; Figure S6: Rietveld refinement results of calcined at 700 °C in air LCNO_01_700 sample; Figure S7: Weight loss curve obtained by TGA for LCNO_01_q sample. Figure S8: EDS mapping patterns of Ca, Ni and La for LCNO_01_q sample—(a,b). Figure S9: HRTEM image of LCNO_01_q sample—(a); occasional stacking faults in the lattice of LCNO_01_q sample—(b). Figure S10: HRTEM images of LCNO_01_t sample showing amorphization and nano-sized particles on the surface as well as disorientated planar defects—(a,b). Figure S11: HRTEM images LCNO_01 sample showing ordered planar defects—(a,b).

Author Contributions: D.M.: Methodology, Formal Analysis, Investigation, Writing—Original Draft; Z.V.: Methodology, Formal Analysis, Investigation, Writing—Original Draft; E.G.: Formal Analysis, Investigation; E.F.: Validation, Writing—Review and Editing; A.S.: Conceptualization, Validation, Supervision; E.P.: Conceptualization, Validation, Writing—Review and Editing, Supervision. All authors have read and agreed to the published version of the manuscript.

Funding: The reported study was funded within the framework of budget project for Synchrotron radiation facility SKIF, Boreskov Institute of Catalysis. In the part of samples characterization by HRTEM technique the work was supported by the Ministry of Science and Higher Education of the Russian Federation within the governmental order for Boreskov Institute of Catalysis.

Institutional Review Board Statement: Not applicable.

Informed Consent Statement: Not applicable.

Data Availability Statement: Data is contained within the article and Supplementary Materials.

Acknowledgments: The HRTEM and TGA study was carried out using facilities of the shared research center “National center of investigation of catalysts” at Boreskov Institute of Catalysis. The synchrotron XRD experiments were performed at the shared research center SSTRC on the basis of the Novosibirsk VEPP-3 complex at BINP SB RAS. The authors thank Alena A. Pochtar’ for providing TGA data. The authors thank Alexander Dmitriev for the article proofreading.

Conflicts of Interest: The authors declare no conflict of interest.

References

1. Xu, X.; Pan, Y.; Zhong, Y.; Ran, R.; Shao, Z. Ruddlesden–Popper Perovskites in Electrocatalysis. *Mater. Horiz.* **2020**, *7*, 2519–2565. [[CrossRef](#)]
2. Liu, P.; Han, N.; Wang, W.; Ran, R.; Zhou, W.; Shao, Z. High-Quality Ruddlesden–Popper Perovskite Film Formation for High-Performance Perovskite Solar Cells. *Adv. Mater.* **2021**, *33*, 2002582. [[CrossRef](#)] [[PubMed](#)]
3. Tarasova, N.; Animitsa, I. Materials $\text{A}^{\text{II}}\text{LnInO}_4$ with Ruddlesden–Popper Structure for Electrochemical Applications: Relationship between Ion (Oxygen-Ion, Proton) Conductivity, Water Uptake, and Structural Changes. *Materials* **2021**, *15*, 114. [[CrossRef](#)] [[PubMed](#)]
4. Ghorbani-Moghadam, T.; Kompany, A.; Golmohammad, M. Study of Structural, Electrical and Electrochemical Properties of $\text{La}_{0.7}\text{Sr}_{1.3}\text{Co}_{1-x}\text{Fe}_x\text{O}_4$ ($x = 0, 0.1, 0.3, 0.5$) Ruddlesden–Popper Oxides as Promising Cathode for Intermediate Solid Oxide Fuel Cells. *J. Alloy. Compd.* **2022**, *900*, 163382. [[CrossRef](#)]
5. Nirala, G.; Yadav, D.; Upadhyay, S. Ruddlesden–Popper Phase A_2BO_4 Oxides: Recent Studies on Structure, Electrical, Dielectric, and Optical Properties. *J. Adv. Ceram.* **2020**, *9*, 129–148. [[CrossRef](#)]
6. Tarutin, A.P.; Lyagaeva, J.G.; Medvedev, D.A.; Bi, L.; Yaremchenko, A.A. Recent Advances in Layered $\text{Ln}_2\text{NiO}_{4+\delta}$ Nickelates: Fundamentals and Prospects of Their Applications in Protonic Ceramic Fuel and Electrolysis Cells. *J. Mater. Chem. A* **2021**, *9*, 154–195. [[CrossRef](#)]
7. Ding, P.; Li, W.; Zhao, H.; Wu, C.; Zhao, L.; Dong, B.; Wang, S. Review on Ruddlesden–Popper Perovskites as Cathode for Solid Oxide Fuel Cells. *J. Phys. Mater.* **2021**, *4*, 022002. [[CrossRef](#)]

8. Sadykov, V.A.; Sadovskaya, E.M.; Ereemeev, N.F.; Pikalova, Y.E.; Bogdanovich, N.M.; Filonova, E.A.; Krieger, T.A.; Fedorova, Y.E.; Krasnov, A.V.; Skriabin, P.I.; et al. Novel Materials for Solid Oxide Fuel Cells Cathodes and Oxygen Separation Membranes: Fundamentals of Oxygen Transport and Performance. *Carbon Resour. Convers.* **2020**, *3*, 112–121. [[CrossRef](#)]
9. Shen, Y.; Zhao, H.; Świerczek, K.; Du, Z.; Xie, Z. Lattice Structure, Sintering Behavior and Electrochemical Performance of $\text{La}_{1.7}\text{Ca}_{0.3}\text{Ni}_{1-x}\text{Cu}_x\text{O}_{4+\delta}$ as Cathode Material for Intermediate-Temperature Solid Oxide Fuel Cell. *J. Power Sources* **2013**, *240*, 759–765. [[CrossRef](#)]
10. Khandale, A.P.; Bansod, M.G.; Bhoga, S.S. Improved Electrical and Electrochemical Performance of Co-Doped $\text{Nd}_{1.8}\text{Sr}_{0.2}\text{Ni}_{1-x}\text{Cu}_x\text{O}_{4+\delta}$. *Solid State Ion.* **2015**, *276*, 127–135. [[CrossRef](#)]
11. Myung, J.; Shin, T.H.; Huang, X.; Savaniu, C.; Irvine, J. $\text{La}_{1.7}\text{Ca}_{0.3}\text{Ni}_{0.75}\text{Cu}_{0.25}\text{O}_{4-\delta}$ -Layered Perovskite as Cathode on $\text{La}_{0.9}\text{Sr}_{0.1}\text{Ga}_{0.8}\text{Mg}_{0.2}\text{O}_3$ or $\text{Ce}_{0.8}\text{Gd}_{0.2}\text{O}_2$ Electrolyte for Intermediate Temperature Solid Oxide Fuel Cells. *Int. J. Appl. Ceram. Technol.* **2016**, *13*, 269–273. [[CrossRef](#)]
12. Pikalova, E.; Kolchugin, A.; Filonova, E.; Bogdanovich, N.; Pikalov, S.; Ananyev, M.; Molchanova, N.; Farlenkov, A. Validation of Calcium-Doped Neodymium Nickelates as SOFC Air Electrode Materials. *Solid State Ion.* **2018**, *319*, 130–140. [[CrossRef](#)]
13. Bhoga, S.S.; Khandale, A.P.; Pahune, B.S. Investigation on $\text{Pr}_{2-x}\text{Sr}_x\text{NiO}_{4+\delta}$ ($x = 0.3\text{--}1.0$) Cathode Materials for Intermediate Temperature Solid Oxide Fuel Cell. *Solid State Ion.* **2014**, *262*, 340–344. [[CrossRef](#)]
14. Gilev, A.R.; Kiselev, E.A.; Cherepanov, V.A. Performance of the Lanthanum Gallate Based Solid Oxide Fuel Cells with the $\text{La}_{2-x}\text{Ca}_x\text{Ni}_{1-y}\text{Fe}_y\text{O}_{4+\delta}$ Cathodes and $\text{Sr}_2\text{Ni}_{0.75}\text{Mg}_{0.25}\text{MoO}_{6-\delta}$ Anode. *Solid State Ion.* **2019**, *339*, 115001. [[CrossRef](#)]
15. Lee, K.-J.; Seo, J.-U.; Lim, Y.-S.; Hwang, H.-J. Electrochemical Performance of a $\text{Nd}_{2-x}\text{Sr}_x\text{NiO}_{4+\delta}$ /GDC ($x = 0, 0.4, 0.6$) as a SOFC Cathode Material. *J. Korean Ceram. Soc.* **2014**, *51*, 51–56. [[CrossRef](#)]
16. Pikalova, E.; Kolchugin, A.; Bogdanovich, N.; Medvedev, D.; Lyagaeva, J.; Vedmid, L.; Ananyev, M.; Plaksin, S.; Farlenkov, A. Suitability of $\text{Pr}_{2-x}\text{Ca}_x\text{NiO}_{4+\delta}$ as Cathode Materials for Electrochemical Devices Based on Oxygen Ion and Proton Conducting Solid State Electrolytes. *Int. J. Hydrog. Energy* **2020**, *45*, 13612–13624. [[CrossRef](#)]
17. Ma, J.; Pan, Y.; Wang, Y.; Chen, Y. A Sr and Ni Doped Ruddlesden–Popper Perovskite Oxide $\text{La}_{1.6}\text{Sr}_{0.4}\text{Cu}_{0.6}\text{Ni}_{0.4}\text{O}_{4+\delta}$ as a Promising Cathode for Protonic Ceramic Fuel Cells. *J. Power Sources* **2021**, *509*, 230369. [[CrossRef](#)]
18. Danilov, N.; Lyagaeva, J.; Vdovin, G.; Pikalova, E.; Medvedev, D. Electricity/Hydrogen Conversion by the Means of a Protonic Ceramic Electrolysis Cell with $\text{Nd}_2\text{NiO}_{4+\delta}$ -Based Oxygen Electrode. *Energy Convers. Manag.* **2018**, *172*, 129–137. [[CrossRef](#)]
19. Li, X.; Huan, D.; Shi, N.; Yang, Y.; Wan, Y.; Xia, C.; Peng, R.; Lu, Y. Defects Evolution of Ca Doped $\text{La}_2\text{NiO}_{4+\delta}$ and Its Impact on Cathode Performance in Proton-Conducting Solid Oxide Fuel Cells. *Int. J. Hydrog. Energy* **2020**, *45*, 17736–17744. [[CrossRef](#)]
20. Pikalova, E.Y.; Kolchugin, A.A. The Influence of the Substituting Element ($M = \text{Ca}, \text{Sr}, \text{Ba}$) in $\text{La}_{1.7}\text{M}_{0.3}\text{NiO}_{4+\delta}$ on the Electrochemical Performance of the Composite Electrodes. *Eur. Chem. Tech. J.* **2016**, *18*, 3. [[CrossRef](#)]
21. Mather, G.C.; Muñoz-Gil, D.; Zamudio-García, J.; Porrás-Vázquez, J.M.; Marrero-López, D.; Pérez-Coll, D. Perspectives on Cathodes for Protonic Ceramic Fuel Cells. *Appl. Sci.* **2021**, *11*, 5363. [[CrossRef](#)]
22. Demourgues, A.; Wattiaux, A.; Grenier, J.C.; Pouchard, M.; Soubeyroux, J.L.; Dance, J.M.; Hagenmuller, P. Electrochemical Preparation and Structural Characterization of $\text{La}_2\text{NiO}_{4+\delta}$ Phases ($0 \leq \delta \leq 0.25$). *J. Solid State Chem.* **1993**, *105*, 458–468. [[CrossRef](#)]
23. Jorgensen, J.D.; Dabrowski, B.; Pei, S.; Richards, D.R.; Hinks, D.G. Structure of the Interstitial Oxygen Defect in $\text{La}_2\text{NiO}_{4+\delta}$. *Phys. Rev. B* **1989**, *40*, 2187–2199. [[CrossRef](#)] [[PubMed](#)]
24. Singh, K.K.; Ganguly, P.; Goodenough, J.B. Unusual Effects of Anisotropic Bonding in Cu(II) and Ni(II) Oxides with K_2NiF_4 Structure. *J. Solid State Chem.* **1984**, *52*, 254–273. [[CrossRef](#)]
25. Ganguly, P.; Rao, C.N.R. Crystal Chemistry and Magnetic Properties of Layered Metal Oxides Possessing the K_2NiF_4 or Related Structures. *J. Solid State Chem.* **1984**, *53*, 193–216. [[CrossRef](#)]
26. Flura, A.; Dru, S.; Nicollet, C.; Vibhu, V.; Fourcade, S.; Lebraud, E.; Rougier, A.; Bassat, J.-M.; Grenier, J.-C. Chemical and Structural Changes in Ln_2NiO_4 ($\text{Ln}=\text{La}, \text{Pr}$ or Nd) Lanthanide Nickelates as a Function of Oxygen Partial Pressure at High Temperature. *J. Solid State Chem.* **2015**, *228*, 189–198. [[CrossRef](#)]
27. Shannon, R.D. Revised Effective Ionic Radii and Systematic Studies of Interatomic Distances in Halides and Chalcogenides. *Acta Cryst. A* **1976**, *32*, 751–767. [[CrossRef](#)]
28. Tang, J.P.; Dass, R.I.; Manthiram, A. Comparison of the Crystal Chemistry and Electrical Properties of $\text{La}_{2-x}\text{A}_x\text{NiO}_4$ ($A = \text{Ca}, \text{Sr}$, and Ba). *Mater. Res. Bull.* **2000**, *35*, 411–424. [[CrossRef](#)]
29. Nakamura, T.; Yashiro, K.; Sato, K.; Mizusaki, J. Electronic State of Oxygen Nonstoichiometric $\text{La}_{2-x}\text{Sr}_x\text{NiO}_{4+\delta}$ at High Temperatures. *Phys. Chem. Chem. Phys.* **2009**, *11*, 3055. [[CrossRef](#)]
30. Nakamura, T.; Yashiro, K.; Sato, K.; Mizusaki, J. Oxygen Nonstoichiometry and Defect Equilibrium in $\text{La}_{2-x}\text{Sr}_x\text{NiO}_{4+\delta}$. *Solid State Ion.* **2009**, *180*, 368–376. [[CrossRef](#)]
31. Kim, H.-S.; Yoo, H.-I. Isothermal Onsager Matrices and Acceptor Size Effect on Mass/Charge Transport Properties of $\text{La}_{1.9}\text{A}_{0.1}\text{NiO}_{3.95+\delta}$ ($A = \text{Ca}, \text{Sr}$). *Phys. Chem. Chem. Phys.* **2014**, *16*, 16595–16605. [[CrossRef](#)]
32. Skinner, S. Oxygen Diffusion and Surface Exchange in $\text{La}_{2-x}\text{Sr}_x\text{NiO}_{4+\delta}$. *Solid State Ion.* **2000**, *135*, 709–712. [[CrossRef](#)]
33. Tropin, E.S.; Ananyev, M.V.; Farlenkov, A.S.; Khodimchuk, A.V.; Berenov, A.V.; Fetisov, A.V.; Eremin, V.A.; Kolchugin, A.A. Surface Defect Chemistry and Oxygen Exchange Kinetics in $\text{La}_{2-x}\text{Ca}_x\text{NiO}_{4+\delta}$. *J. Solid State Chem.* **2018**, *262*, 199–213. [[CrossRef](#)]
34. Kolchugin, A.A.; Pikalova, E.Y.; Bogdanovich, N.M.; Bronin, D.I.; Pikalov, S.M.; Plaksin, S.V.; Ananyev, M.V.; Eremin, V.A. Structural, Electrical and Electrochemical Properties of Calcium-Doped Lanthanum Nickelate. *Solid State Ion.* **2016**, *288*, 48–53. [[CrossRef](#)]

35. Sadykov, V.A.; Sadovskaya, E.M.; Pikalova, E.Y.; Kolchugin, A.A.; Filonova, E.A.; Pikalov, S.M.; Ereemeev, N.F.; Ishchenko, A.V.; Lukashevich, A.I.; Bassat, J.M. Transport Features in Layered Nickelates: Correlation between Structure, Oxygen Diffusion, Electrical and Electrochemical Properties. *Ionics* **2018**, *24*, 1181–1193. [[CrossRef](#)]
36. Pikalova, E.; Sadykov, V.; Sadovskaya, E.; Yeremeev, N.; Kolchugin, A.; Shmakov, A.; Vinokurov, Z.; Mishchenko, D.; Filonova, E.; Belyaev, V. Correlation between Structural and Transport Properties of Ca-Doped La Nickelates and Their Electrochemical Performance. *Crystals* **2021**, *11*, 297. [[CrossRef](#)]
37. Du, Z.; Zhang, Z.; Niemczyk, A.; Olszewska, A.; Chen, N.; Świerczek, K.; Zhao, H. Unveiling the Effects of A-Site Substitutions on the Oxygen Ion Migration in $A_{2-x}A'_xNiO_{4+\delta}$ by First Principles Calculations. *Phys. Chem. Chem. Phys.* **2018**, *20*, 21685–21692. [[CrossRef](#)]
38. Shen, Y.; Zhao, H.; Liu, X.; Xu, N. Preparation and Electrical Properties of Ca-Doped $La_2NiO_{4+\delta}$ Cathode Materials for IT-SOFC. *Phys. Chem. Chem. Phys.* **2010**, *12*, 15124. [[CrossRef](#)]
39. Poirrot, N.; Zaghrioui, M. Synthesis and Characterization of Calcium-Doped Lanthanum Nickelates $La_{2-x}Ca_xNiO_{4+\delta}$ (). *Solid State Sci.* **2006**, *8*, 149–154. [[CrossRef](#)]
40. Shi, C.-Y.; Hu, Z.-B.; Hao, Y.-M. Structural, Magnetic and Dielectric Properties of $La_{2-x}Ca_xNiO_{4+\delta}$ ($x = 0, 0.1, 0.2, 0.3$). *J. Alloy. Compd.* **2011**, *509*, 1333–1337. [[CrossRef](#)]
41. Piminov, P.A.; Baranov, G.N.; Bogomyagkov, A.V.; Berkaev, D.E.; Borin, V.M.; Dorokhov, V.L.; Karnae, S.E.; Kiselev, V.A.; Levichev, E.B.; Meshkov, O.I.; et al. Synchrotron Radiation Research and Application at VEPP-4. *Phys. Procedia* **2016**, *84*, 19–26. [[CrossRef](#)]
42. Aulchenko, V.M.; Evdokov, O.V.; Kutovenko, V.D.; Pirogov, B.Y.; Sharafutdinov, M.R.; Titov, V.M.; Tolochko, B.P.; Vasiljev, A.V.; Zhogin, I.A.; Zhulanov, V.V. One-Coordinate X-Ray Detector OD-3M. *Nucl. Instrum. Methods Phys. Res. Sect. A Accel. Spectrometers Detect. Assoc. Equip.* **2009**, *603*, 76–79. [[CrossRef](#)]
43. Toby, B.H.; Von Dreele, R.B. GSAS-II: The Genesis of a Modern Open-Source All Purpose Crystallography Software Package. *J. Appl. Cryst.* **2013**, *46*, 544–549. [[CrossRef](#)]
44. Stephens, P.W. Phenomenological Model of Anisotropic Peak Broadening in Powder Diffraction. *J. Appl. Cryst.* **1999**, *32*, 281–289. [[CrossRef](#)]
45. Rodríguez-Carvajal, J.; Fernández-Díaz, M.T.; Martínez, J.L. Neutron Diffraction Study on Structural and Magnetic Properties of La_2NiO_4 . *J. Phys. Condens. Matter* **1991**, *3*, 3215–3234. [[CrossRef](#)]
46. Rodríguez-Carvajal, J. Recent Advances in Magnetic Structure Determination by Neutron Powder Diffraction. *Phys. B: Condens. Matter* **1993**, *192*, 55–69. [[CrossRef](#)]
47. Boulle, A.; Legrand, C.; Guinebretière, R.; Mercurio, J.P.; Dauter, A. Planar Faults in Layered Bi-Containing Perovskites Studied by X-ray Diffraction Line Profile Analysis. *J. Appl. Cryst.* **2001**, *34*, 699–703. [[CrossRef](#)]
48. Olikhovska, L.; Ustinov, A. Diffraction Analysis of Perovskite-like Oxides Containing Irregular Intergrowths. *J. Appl. Cryst.* **2009**, *42*, 1–9. [[CrossRef](#)]
49. Tonus, F.; Bahout, M.; Battle, P.D.; Hansen, T.; Henry, P.F.; Roisnel, T. In Situ Neutron Diffraction Study of the High-Temperature Redox Chemistry of $Ln_{3-x}Sr_{1+x}CrNiO_{8-\delta}$ ($Ln = La, Nd$) under Hydrogen. *J. Mater. Chem.* **2010**, *20*, 4103. [[CrossRef](#)]
50. Gilev, A.R.; Kiselev, E.A.; Cherepanov, V.A. Homogeneity Range, Oxygen Nonstoichiometry, Thermal Expansion and Transport Properties of $La_{2-x}Sr_xNi_{1-y}Fe_yO_{4+\delta}$. *RSC Adv.* **2016**, *6*, 72905–72917. [[CrossRef](#)]
51. Aguadero, A.; Escudero, M.J.; Pérez, M.; Alonso, J.A.; Pomjakushin, V.; Daza, L. Effect of Sr Content on the Crystal Structure and Electrical Properties of the System $La_{2-x}Sr_xNiO_{4+\delta}$ ($0 \leq x \leq 1$). *Dalton Trans.* **2006**, 4377–4383. [[CrossRef](#)] [[PubMed](#)]